Eliminating object prior-bias from sparse-projection tomographic reconstructions

Preeti Gopal, Sharat Chandran, Imants Svalbe, and Ajit Rajwade

***Abstract*—Tomographic reconstruction from undersampled measurements is a necessity when the measurement process is potentially harmful, needs to be rapid, or is resource-expensive. In such cases, information from previously existing longitudinal scans of the same object ('object-prior') helps in the reconstruction of the current object ('test') from its significantly fewer measurements. A common problem with these techniques is the strong influence of object-priors in the reconstruction of new regions in the test. In this work, we mitigate this problem by first estimating the location of new regions and then imposing object-prior in *only* the other old regions which are similar to the prior.**

Our work is based on longitudinal data acquisition scenarios where we wish to study new changes that evolve within an object over time, such as in repeated scanning for disease monitoring, or in tomography-guided surgical procedures. While this is easily feasible when measurements are acquired from a large number of projection angles ('views'), it is challenging when the number of views is limited (sub-Nyquist). We show that in the latter case, a 'spatially-varying' technique is appropriate in order to prevent the prior from adversely affecting the reconstruction of new structures that are absent in any of the earlier scans. The reconstruction of new regions is safeguarded from the bias of the prior by computing regional weights that moderate the local influence of the priors. We are thus able to effectively reconstruct both the old and the new structures in the test. We have tested the efficacy of our method on synthetic as well as real projection data, in both 2D and 3D. Our method significantly improves the overall quality of reconstructions while minimizing the number of measurements needed for imaging in longitudinal studies.

***Index Terms*—Limited-view tomographic reconstruction, regularization priors, object priors, longitudinal studies.**

I. Introduction

Computed Tomography (CT) deals with the recovery of details of an object's interior from a limited set of projection data acquired by passing X-rays at different orientations ('views'). It is preferable to minimize the radiation exposed in order to prevent any potential damage to it and in order to reduce the acquisition time. Therefore, current research seeks to either significantly reduce the radiation intensity required to reconstruct with adequate fidelity [1], [2], [3], [4] or significantly reduce the number of measurements required to reconstruct with adequate fidelity. For the latter case, there are two lines of pursuit. One is to intelligently choose those sets of projection views that capture most information [5], [6], [7], [8], [9], and the other, which is the focus of this paper, is to design the reconstruction algorithm in order to achieve the most accurate recovery of the underlying slice, given the measurements from any limited set of views [1], [10], [11].

In conventional data acquisition techniques, tomographic measurements $\boldsymbol{y}$ are acquired by sampling the physical object $\boldsymbol{x}$ uniformly with a substantial number of views, ideally above the Nyquist rate. In such a case when there are sufficient measurements, reconstruction using conventional filtered back-projection (FBP) suffices, as seen in Fig. 1 (first column, 800 views). The figure shows the ground truth image (260×260) of naturally growing sprouts at the top left (the details of this dataset is postponed to Section IV).

However, reconstruction from reduced views has been made possible by assuming the data to exhibit certain properties such as smoothness in image space, sparsity in gradient space [12] or sparsity under certain mathematical transforms [13], [14] such as the Discrete Cosine Transform (DCT). There are multiple such regularization priors, of which we choose the total Variation (TV) method as a baseline for this work. If $\boldsymbol{\mathcal{R}}$ represents the acquisition model, then TV-regularized solution is described by one that minimizes a combination of least squares error and TV-norm of the object $\boldsymbol{x}$. This is described by

$$J_{TV}(\boldsymbol{x}) = \|\boldsymbol{\mathcal{R}}\boldsymbol{x} - \boldsymbol{y}\|_2^2 + \lambda_{TV} TV(\boldsymbol{x}) \tag{1}$$

where the TV-norm is given by

$$TV(\boldsymbol{x}) = \sum_{i,j} \nabla_{ij}(\boldsymbol{x}), \tag{2}$$

and ∇ represents the gradient operator.

Fig. 1 (second column) demonstrates the benefit of using a regularization prior when the number of projection views is limited (100 views). We solve this cost function using an optimal first-order method for large-scale TV regularization presented in [15] and available in [16].

When the number of views is significantly reduced (this paper), a regularization prior alone is not sufficient. In such cases additional information ('object-prior') specific to the current object being scanned (called the 'test' henceforth) is useful in further improving the reconstruction. While this has been done in the context of dynamic CT-scans (discussed more in Section II), in this paper we use a set S of previous scans of the same object. This is relevant in a longitudinal context: the acquisition of sequential CT scans of the same subject in order to track time-evolving changes within the subject's interior. As seen in Fig. 1 (last column, 20 views) our method uses the set S by creating an eigenspace representation (Section V).

Preeti Gopal is with IITB-Monash Research Academy

Sharat Chandran and Ajit Rajwade are with the Department of Computer Science and Engineering, IIT Bombay

Imants Svalbe is with the School of Physics and Astronomy, Monash University

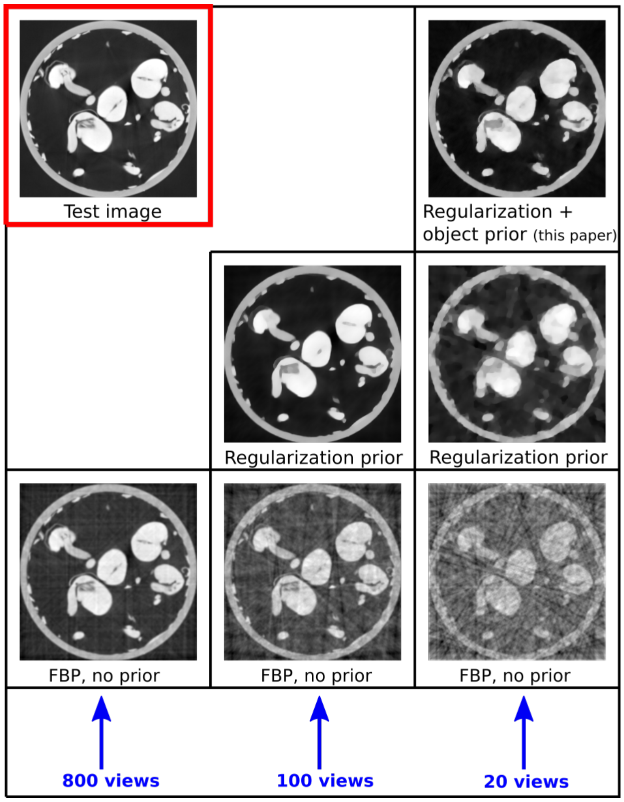

Fig. 1: Illustration of the use of various priors in reconstruction as the number of views reduces. For all cases, the ground truth (260×260) appears in the top left. For extremely large number of views (800 views), FBP reconstruction (first column) is of very good quality (Structural Similarity Index Metric, SSIM=0.92). As the number of views become limited (100 views), reconstruction using Total Variation (TV, middle column) is better both visually and quantitatively than FBP (SSIM of 0.96 vs 0.82). If the number of views is drastically reduced (20 views), the presence of both TV prior and object- prior together improves the reconstruction (SSIM=0.91) when compared to presence of only TV prior (SSIM=0.87) or no prior (SSIM=0.64).

With the use of an object-prior, a new challenge emerges. The prior set S may potentially overwhelm the necessary details, and when several prior scans are available, finding the right one is an issue. We therefore devise an algorithm that estimates the location and magnitude of new changes in the (unknown) test. As we show in Section V, this eventually prevents the prior from adversely affecting the reconstruction of new regions in the test. We refer to this method as a *spatially-varying* prior-based reconstruction routine, that still uses *all* the previous scans in the set S, without using any of the prior scans *as is*, or endeavoring to choose one "right" prior.

This paper is organized as follows. After discussing related work in Section II, Section III lays down the key contributions of this work. Details of the datasets created and used for validation are described in Section IV. Section VI-A demonstrates the utility of our method on a longitudinal medical dataset. We now move to the details. Section V describes computation of a spatially-varying weights map in order to preserve new changes in the test. Results are presented in Section VI. Section VII discusses tuning of the hyperparameters involved, and limitations of our method. Finally, we conclude with key inferences that can be drawn from our work in Section VIII.

II. Related Work

The idea of using a reduced number of views is most pronounced in specialized applications. For example, in [17], sparsity-constrained optimization is presented for angiography. Here, the regions of interest are the vessels alone and they are highlighted by physically inserting a contrast agent, and therefore there is an inherent sharper contrast between the vessels and the background. In other applications where the spatial-gradient of the underlying volume is known to be sparse, the 'total variation' method, as used in [18], [19], can be applied. However, as shown earlier in Fig. 1, these regularization priors are not sufficient when very few views are acquired, thus needing information from stronger priors such as those obtained from previous scans of the same or similar object.

Most object-prior based reconstruction have been in the areas of dynamic CT and 4D-CT. The object-prior usually consists of an object reconstructed to high quality from a large number of projection angles. One of the earliest pieces of work in this area is the well-cited PICCS method [20] for dynamic CT, which enforces a robust-norm based similarity between the test and the object prior, in addition to a sparsity prior on the test. Its limitation is the unchecked over-emphasis of the prior on the reconstruction of the test at hand. A closely related method called PIRPLE was proposed in [21], with additional steps to register the object prior and the test and a somewhat more flexible combination of data fidelity terms, sparsity prior and object prior. However, this method too has similar limitations as PICCS.

In order to prevent the object-prior from overwhelming the reconstruction of test, a few other approaches have either estimated the motion between the object-prior and the test or have applied very specific object-properties for identifying new changes in test. Examples for the former include [22], where changes across the successive scan volumes are assumed to be continuous, thus enabling the use of optical flow to model the motion between corresponding voxels of different scan volumes. In another study [23], changes between successive scans were modelled by affine deformation whose parameters were computed for motion-correction, which inturn enables acquisition from fewer views. In [24], all the scan volumes are reconstructed together using spatio-temporal regularization. Here again, the inherent assumption is the continuity across volumes in space or time.

The methods that use object-specific knowledge are [25] and [26]. In [25], knowledge of attenuation coefficient of the fluid is used as a prior for reconstructing its flow through gravel. However, this relies on additional expert domain knowledge which may not be available or which may be infeasible to acquire. Other approaches variously use robust principal components analysis assuming that the object consists of a large static part (background) and a sparse moving part (foreground) [27], spline-based models for tracking the regions of change in an SIRT framework [28].

All of these techniques [24], [22], [25], [27], [28] essentially reconstruct all the different stages of the object *simultaneously*, and use the extra redundancy across time simultaneously. In the scenario of a longitudinal study (where projection measurements are acquired at instants that are several weeks apart) which we consider in this paper, such approaches are not feasible. A longitudinal study will necessarily require reconstructions soon after acquisition of each set of measurements.

There also exist methods for estimating new changes (in the test) directly in projection space. In such techniques which can be used in longitudinal studies, the object-prior is projected in the same set of views as the current set of test measurements, and a set of projection differences is computed. These projection differences are essentially tomographic projections of differences between the unknown test and the known object-prior. Hence, a variety of reconstruction algorithms can be used to estimate such a difference image which can then be added to the object-prior to yield the final estimate of the test. Such methods have been proposed in [29], [30]. However, reconstruction of the difference image will inherently contain sub-sampling artefacts, and these artefacts will appear in the final reconstruction as there is no mechanism to mitigate them (unlike the method that we propose). This can be seen in Sec. 4 of our supplementary material [31], where we have compared our method with [30].

In this paper, we present a technique that makes use of multiple object priors, corresponding to high quality reconstructions of similar objects across time, typically in a longitudinal study. We use these priors to improve the reconstruction of the test from largely undersampled measurements. In particular, we define regions of change between the test and the eigenspace spanned by previous high quality object-priors in a purely data driven manner. Additionally, our technique differentiates between genuine structural changes and “changes” that appear due to undersampling artefacts (as seen in Sec.4 of our supplementary material [31]). Besides this, since we use a statistical model with multiple object-priors, we avoid the problem of selecting an appropriate single object-prior unlike [20], [29], [30], [21], [26] and also make use of the additional information available in multiple priors. Our technique also has the advantage of not requiring any expert-domain knowledge about the object being scanned.

III. Contributions

This paper focusses on few-views reconstruction with an emphasis on longitudinal studies. In contrast to the object-prior based studies mentioned above, we reconstruct the current test object without any assumption of continuity of changes or knowledge of the attenuation coefficients of the structures. We also do not make any temporal assumption in terms of time intervals – prior scans could be months apart. We use the current measurements from few-views and previous scans of the same object. A key idea in our work is this starting point – the new test volume is close to the space spanned by the eigenvectors of multiple representative previously scanned objects.

We discuss the danger in imposing an inflexible constant weight (and hence an unnecessary bias) when reconstructing the data. As a solution, we present a method to moderate the control of the prior by estimating and imposing spatially-varying weights to the prior in order to reconstruct new structures accurately. This spatially-varying prior tunes the effect of the templates in different regions of the reconstruction.

Fig. 2 provides an overview.

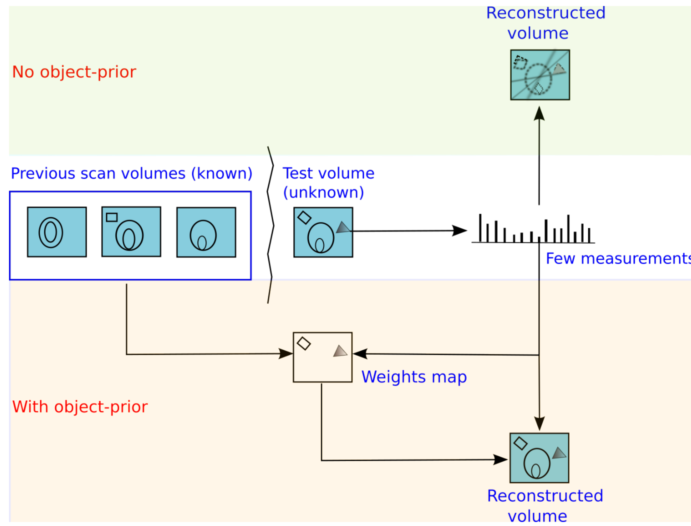

Fig. 2: Overview of our work. When the number of measurements is lower than what is conventionally used, (a) a regularization prior (such as Total Variation) alone is not sufficient to mitigate the sub-sampling artefacts. (b) An object-prior must be used to provide additional information. Here, in order to prevent a prior induced bias in the reconstruction, we propose using a spatially-varying weights-map to modulate the effect of object-prior on the final reconstruction.

In summary, the key contributions are

- We create new 3D biological datasets (Section IV) and present results on real cone-beam projections. Our datasets and code will be made available to the community.
- We design a weights-map to depict the location and strength of new changes in the test at every voxel. A novel algorithm is presented to build this map from sub-sampled measurements of the test and a set of high quality templates. Once the weights-map is built, it is used for accurate reconstruction of those changes in the test that are absent in all of the templates. Results appear in Section VI.
- We show the efficacy of our results in a real-life medical longitudinal study with data obtained in a clinical setting from a live teaching and research hospital.

IV. Datasets

In this section, we lay the details of all the real and simulated datasets created and used for this work. The first 3 datasets: Okra, Potato and Sprouts were acquired from the Australian National University (ANU). We wish to emphasize that data from commercially available CT machines may not be suitable because most CT scanners do not reveal the raw measurements, and instead output only the full reconstructed volumes. Moreover, the process of conversion from the projections to the full volumes is proprietary. Departing from this, we demonstrate reconstruction results (in Section VI from the following datasets.

Liver: This data was sourced from Tata Memorial Centre [32] in Parel, Mumbai. This is the national comprehensive centre for the prevention, treatment, education and research in cancer, and is recognized as one of the leading cancer centres in India. The dataset (Fig. 3) from this longitudinal medical study consists of 7 scans taken at different stages of radio-frequency ablation study of a liver. In such a procedure [33], the physician inserts a thin needle-like probe into the organ. Repeated CT scans of the patient are acquired in order to track the movement of the needle and to ensure that it is reaching the appropriate target tumor. Once the needle hits the tumor, a high-frequency electric current is passed through the tip of the probe and this burns the malignant tumor (ablation).

In our experiments, we generate parallel beam measurements from 2D slices from each of the 7 volumes. Note that all these 7 slices are located at the *same* index (slice number corresponding to the same depth) within each of the respective volumes. Observe (in Fig. 3) that the needle is seen in all of the 7 slices.

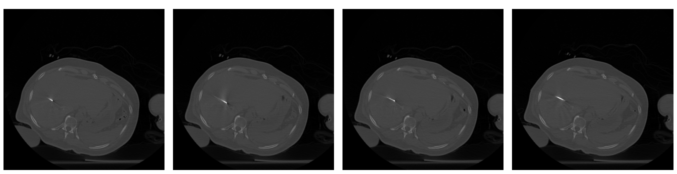

(a) slice 1 (b) slice 2 (c) slice 3 (d) slice 4

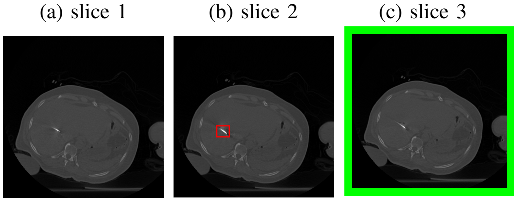

(e) slice 5 (f) slice 6 (g) slice 7

Fig. 3: Radio-frequency ablation dataset: One of the slices (512×512) from each of the 7 scan volumes of a longitudinal study dataset of the liver. Note that in volumes (a) through (g), the needle (shown in red in (f)) approaches the target tumor.

Okra: This dataset is that of an Okra specimen consisting of its five scans (Fig. 4). Prior to the first scan, two cuts were drilled on the surface of the specimen. This was followed by four scans, each after introducing one new cut. The specimen was kept in the same position throughout the acquisitions. The measurements consisted of real circular cone-beam projections from 450 views, each of size 336×156. In our experiments, the first 4 volumes shown in Fig. 4 were used to build the object-prior and the last volume was used as the test. The ground truth consists of volumes of size 338×338×123 reconstructed using the Feldkamp-Davis-Kress (FDK) algorithm [34] from the full set of 450 view projections.

Sprouts: This 3D dataset, which was also obtained at ANU, consists of six reconstructed volumes corresponding to six scans of an in-vivo sprout specimen imaged at its various stages of growth (Fig. 5). *In contrast to the scientific experiment performed for the case of the okra and potato where we introduced man-made defects, the changes here*

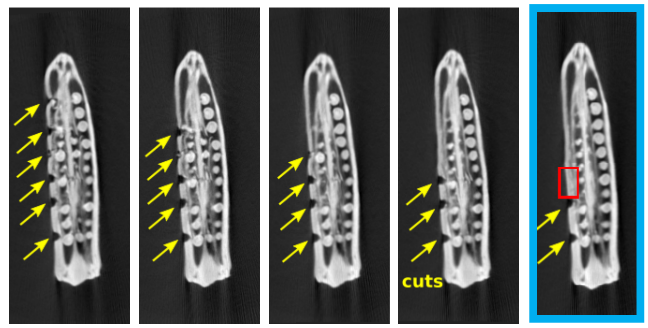

Fig. 4: Okra 3D dataset: One slice each from the scanned objects that are used as object-prior (the first four from left) and a slice from the test volume (extreme right). Notice the region marked in red box; while all slices have deformities here, the test has none.

are purely the work of nature. In our experiments, the first 5 volumes were used to build the object-prior and the last volume was used as the test. The ground truth consists of FDK reconstructed volumes of size 130×130×130 from a set of 1800 view projections. For the test, cone-beam projections were generated from the test volume.

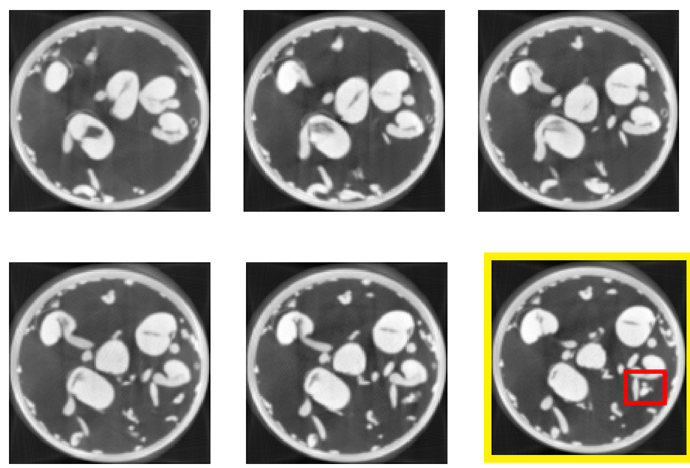

Fig. 5: Sprouts 3D dataset: One slice each from the previously scanned objects (the first five from left) and a slice from the test (extreme right). Notice the structure within the red box in the test that is different from all of the other images.

Potato: This dataset consisted of four scans of the humble potato (Fig. 6). While the first scan was taken of the undistorted potato, subsequent scans were taken of the same specimen, each time after drilling a new hole halfway into the potato. Measurements from each scan consisted of real circular cone-beam projections from 900 views, each of size 150×150. every update of the reconstructed test volume. In our experiments, the first 3 volumes were used to build the object-prior and the last volume was used as the test. The ground truth consists of volumes of size 150×150×100 reconstructed using FDK from the full set of 900 projection views.

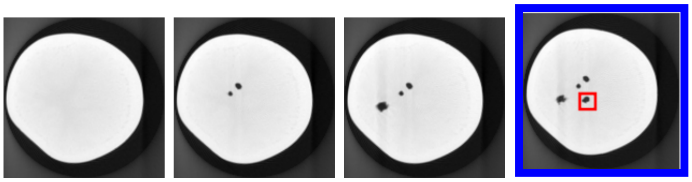

Fig. 6: Potato 3D dataset: One slice each from the previously scanned objects (the first three from left) and a slice from the test volume (extreme right). Notice the appearance of the fourth hole in the test slice.

V. Spatially-Varying prior-based reconstruction

Our method modifies the algorithm presented in [35] and addtionally overcomes one of its major limitations by introducing an extra computational step. We first review the eigenspace-cum-CS prior-based reconstruction algorithm for a 2D uniform prior-based reconstruction, which was shown [35] to be better when compared to dictionary-based priors. PCA has been traditionally used to find the significant modes of (Gaussian corrupted) data. In this regard, it has been widely applied in the context of data compression. However, PCA can also be seen as a tool to provide an orthogonal basis to represent the space in which most of the test data could lie (except the new changes). This space is constructed from the available set of previously scanned objects which must cover a realistically representative range of structures.

To begin with, when an object is scanned multiple times, a set of high quality reconstructions (i.e., reconstructions from a dense set of projection views) may be chosen as object-prior for the reconstruction of future scan volumes, which in turn, may be scanned using far fewer measurements. The eigenspace E_{high} of the L previously scanned objects $Q_1, Q_2, ..., Q_L$ is pre-computed. Here, it is assumed that most of the test volume, barring the new changes, can be expressed as a sparse linear combination of the principal components (eigenvectors of the covariance matrix) obtained from a group of structurally similar volumes. Hence, the object-prior is represented by means of PCA. For the eigenspace to encompass a range of possible structures in the test slice, the object-prior must represent a wide structural range. Moreover, if these volumes are not aligned, then they must be first registered before computing the prior.

The prior is built by computing the covariance matrix from the template set $\{Q_i\}_{i=1}^{L}$. The space spanned by the eigenvectors $\{\boldsymbol{V_k}\}_{k=1}^{L-1}$ (eigenspace) of the covariance matrix is the object prior and is assumed to contain most of the test slice (or volume in the case of 3D) that is similar, but not necessarily identical to the object-prior. We use all of the $L-1$ orthogonal eigenvectors as a basis to represent the unknown test volume. Let $\boldsymbol{\mu}$ denote the mean of the previously scanned objects, and $\boldsymbol{\alpha}$ the unknown vector of eigen-coefficients of the test scan, of which α_k is the k^{th} element. Then, once the eigenspace is pre-computed, the test was reconstructed in [35] by imposing a penalty if the estimated slice does not lie within the eigen-space of the object prior.

Although the uniform prior can be very useful in some circumstances, it poses a limitation when we want accurate details of a portion of the new changes. While the uniform prior compensates very well for the possible artefacts due to sparse measurements, it may dominate the regions with new changes masking the signal. Ideally, we will want to impose the prior only in the regions that are common between the test and object-prior. Our spatially-varying prior based reconstruction overcomes this limitation by minimizing the following cost function:

$$\begin{aligned} J_3(\boldsymbol{x}, \boldsymbol{\alpha}) = & \|\boldsymbol{\mathcal{R}x} - \boldsymbol{y}\|_2^2 + \lambda_1 TV(\boldsymbol{x}) + \\ & \lambda_2 \|\boldsymbol{W}(\boldsymbol{x} - (\boldsymbol{\mu} + \sum_k \boldsymbol{V_k}\alpha_k))\|_2^2. \end{aligned} \tag{3}$$

$$\begin{aligned} J_{\boldsymbol{\alpha}}(\mathbf{x}) \triangleq & \|\boldsymbol{\mathcal{R}x} - \boldsymbol{y}\|_2^2 + \lambda_1 TV(\boldsymbol{x}) \\ & + \lambda_2 \|(\boldsymbol{W}(\boldsymbol{x} - (\boldsymbol{\mu} + \boldsymbol{V\alpha}))\|_2^2 \end{aligned} \tag{4}$$

$$J_{\boldsymbol{x}}(\boldsymbol{\alpha}) \triangleq \|\boldsymbol{W}(\boldsymbol{x} - (\boldsymbol{\mu} + \boldsymbol{V\alpha}))\|_2^2. \tag{5}$$

The key to our method is the discovery of a diagonal weights matrix $\boldsymbol{W}$, where W_{ii} contains the (non-negative) weight assigned to the i^{th} voxel of the prior. $\boldsymbol{W}$ is first constructed using some preliminary reconstruction methods, following which Eq. 3 is used to obtain the final reconstruction. In regions of change in test data, we want lower weights for the prior when compared to regions that are similar to the prior.

λ_1, λ_2 are tunable weights given to the TV-prior and object-prior terms respectively. The unknowns $\mathbf{x}$ and $\boldsymbol{\alpha}$ are solved by alternately minimizing $J_{\boldsymbol{\alpha}}(\mathbf{x})$ using a fixed $\boldsymbol{\alpha}$, and $J_{\boldsymbol{x}}(\boldsymbol{\alpha})$ using the resultant $\mathbf{x}$. $J_{\boldsymbol{\alpha}}(\mathbf{x})$ is solved for using an optimal first-order method for large-scale TV regularization presented in [15] and available in [16]. Solving for $\boldsymbol{\alpha}$ leads to the closed form update:

$$\boldsymbol{\alpha} = [(\boldsymbol{WV})^T \boldsymbol{WV}]^{-1}.\boldsymbol{V}^T(\boldsymbol{W}^T\boldsymbol{W}(\boldsymbol{x} - \boldsymbol{\mu})) \tag{6}$$

The cost function described in Eq. 3 is biconvex and the convergence of this optimization is guaranteed by the monotone convergence theorem [36].

Computation of weights matrix $\boldsymbol{W}$: Since the test is unknown to begin with, it is not possible to decipher the precise regions in $\boldsymbol{x}$ that are different from all the previously scanned objects ('object-prior'). We start with X^{fdk}, the initial backprojection reconstruction of the test volume using FDK in an attempt to discover the difference between the object-prior and the test volume. Let $\boldsymbol{V}_{\text{high}}$ be the eigenspace constructed from high-quality object-prior. However, the difference between X^{fdk} and its projection onto the eigenspace $\boldsymbol{V}_{\text{high}}$ will detect the new regions along with many false positives (false new regions). This is because, X^{fdk} will contain many geometric-specific artefacts arising from sparse measurements (angle undersampling), which are absent in the high quality object-prior used to construct the eigenspace $\boldsymbol{V}_{\text{high}}$. To discover unwanted artefacts of the imaging geometry, in a counter-intuitive way, we generate *low quality* reconstruction of the object-prior as described below.

Algorithm to compute weights-map $\boldsymbol{W}$:

1) Perform a pilot reconstruction X^{fdk} of the test volume $\boldsymbol{x}$ using FDK.

2) Compute low quality template volumes Y^{fdk}. We assume L previously scanned objects from which we build an eigenspace.
   a) Generate simulated measurements $\boldsymbol{y}_{\boldsymbol{Q_i}}$ for every template Q_i, using the exact same projections views and imaging geometry with which the measurements $\boldsymbol{y}$ of the test volume $\boldsymbol{x}$ were acquired, and
   b) Perform L preliminary FDK reconstructions of each of the L object-prior from $\boldsymbol{y}_{\boldsymbol{Q_i}}$. Let this be denoted by $\{Y_i^{\text{fdk}}\}_{i=1}^{L}$.
3) Build eigenspace $\boldsymbol{V}_{\text{low}}$ from $\{Y_i^{\text{fdk}}\}_{i=1}^{L}$. Let P^{fdk} denote projection of X^{fdk} onto $\boldsymbol{V}_{\text{low}}$. The difference between P^{fdk} and X^{fdk} will not contain false positives due to imaging geometry, but will have false positives due to artefacts that are specific to the reconstruction method used. To resolve this, perform steps 4 and 5.
4) Project with multiple methods.
   a) Perform pilot reconstructions of the test using M different reconstruction algorithms like the CS [37], Total Vairiation [12],Algebraic Reconstruction Technique (ART) [38], Simultaneous Algebraic Reconstruction Technique (SART) [39] and Simultaneous Iterative Reconstruction Technique (SIRT) [40]. Let this set of pilot reconstructions be denoted as $X \triangleq \{X^j\}_{j=1}^{M}$ where j is an index for the reconstruction method, and $X^1 = X^{\text{fdk}}$.
   b) From $\boldsymbol{y}_{\boldsymbol{Q_i}}$, perform reconstructions of the template Q_i using the M different algorithms, for each of the L previously scanned objects. Let this set be denoted by $Y \triangleq \{\{Y_i^j\}_{j=1}^{M}\}_{i=1}^{L}$ where $Y_i^1 = Y_i^{\text{fdk}}$, $\forall i \in \{1, .., , L\}$.
   c) For each of the M algorithms (indexed by j), build an eigenspace $\boldsymbol{V}_{\text{low}}^{\boldsymbol{j}}$ from $\{Y_1^j, Y_2^j, \ldots, Y_L^j\}$.
   d) Next, for each j, project X^j onto $\boldsymbol{V}_{\text{low}}^{\boldsymbol{j}}$. Let this projection be denoted by P^j. To reiterate, this captures those parts of the test volume that lie in the subspace $\boldsymbol{V}_{\text{low}}^{\boldsymbol{j}}$ (i.e., are similar to the template reconstructions). The rest, i.e., new changes and their reconstruction method-dependent-artefacts, are not captured by this projection and need to be eliminated.
5) To remove all reconstruction method dependent false positives, we compute $\min_j(|X^j(x,y,z) - P^j(x,y,z)|)$. (The intuition for using the 'min' is provided in the paragraph immediately following step 6 of this procedure.)
6) Finally, the weight to prior for each voxel coordinate (x, y, z) is given by

$$\boldsymbol{W_v}(x,y,z) = (1 + k(\min_j |X^j(x,y,z) - P^j(x,y,z)|))^{-1}. \tag{7}$$

Note that here $\boldsymbol{W_v}(x, y, z)$ represents the weight to the prior in the $(x, y, z)^{th}$ voxel. $\boldsymbol{W_v}(x, y, z)$ must be low whenever the preliminary test reconstruction $X^j(x, y, z)$ is different from its projection $P^j(x, y, z)$ onto the prior eigenspace, for *every* method $j \in \{1, ..., M\}$. This is because it is unlikely that *every* algorithm would produce a significant artefact at a voxel, and hence we hypothesize that the large difference has arisen due to genuine structural changes. The parameter k decides the sensitivity of the weights to the difference $|X^j(x, y, z) - P^j(x, y, z)|$. Selection of k is discussed in detail in Sec. VII.

Motivation for the use of multiple types of eigenspaces for the computation of weights:

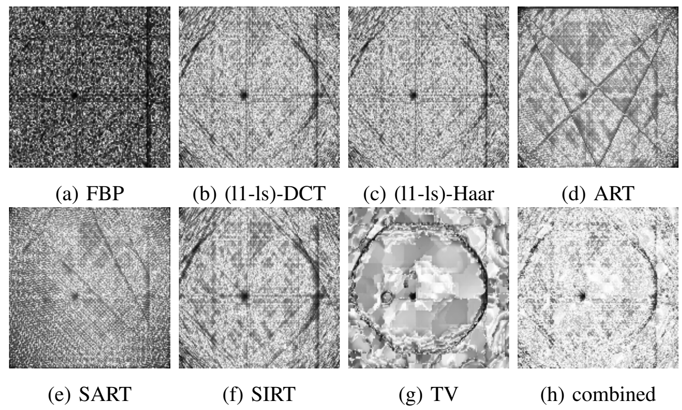

Fig. 7: For reconstruction of the test image in Fig. 6(d) from 6 views, these are the weights-maps (corresponding to the difference between pilot reconstruction of the test and its projection onto the eigenspace $\boldsymbol{V}_{\text{low}}$) constructed using different reconstruction methods individually (a-f) and collectively (g) by fusing information from all reconstruction methods, as specified in Eq. 7. The weights-maps are different because the reconstruction artefacts of the new structures in test image will be different for every reconstruction method used, as seen in Fig. 8.

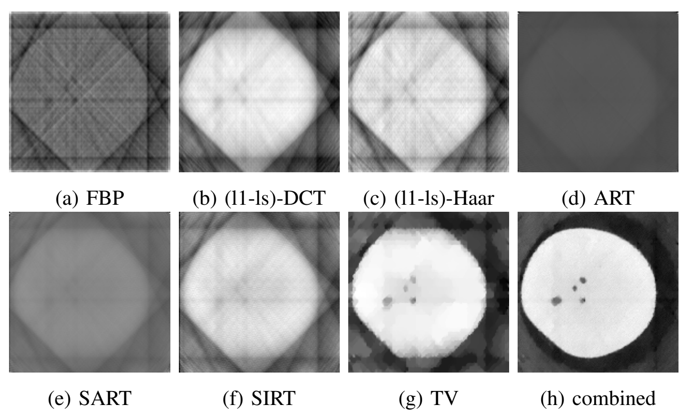

Fig. 8: (a)-(f):Different reconstructions of 6(d) from 6 views. The magnitude and sharpness of the artefacts is different for each method. (g) Spatially-Varying-prior method that combines weights-map information from all other methods. The SSIM of these reconstructions is shown in Table. I.

The changes and new structures present in the test data will generate different artifacts for different reconstruction techniques. These artifacts would not be captured by reconstructions of the object-prior since the underlying new changes and structures may be absent in all of the previously scanned objects. We aim to let the weights be independent of the type of artifact. Hence, we use a combination of different reconstruction techniques to generate different types of eigenspaces and combine information from all of them to compute weights. To illustrate the benefit of this method, we first performed 2D reconstruction of a test slice from the potato dataset. Fig. 6 shows the test and template slices. Fig. 7 shows the weights-maps generated using Eq. 7 by various reconstruction methods. It can be seen that the weights are low in the region of the new change in test data. Because all the iterative methods are computationally expensive, we chose only FBP and TV for computing weights-maps for all 3D reconstructions.

TABLE I: SSIM of the reconstructions shown in Fig. 8:(a)-(g). The SSIM of ground-truth (ideal reconstruction) is 1.

Fig. 8	**(a)**	**(b)**	**(c)**	**(d)**	**(e)**	**(f)**	**(g)**	**(h)**
	0.64	0.72	0.68	0.83	0.81	0.69	0.83	0.88

VI. Results

We present results on 2D and 3D synthetic as well as real tomographic data of biological and medical specimens.

A. *CT-guided radio-ablation study*

We first show how our technique is useful in a real-life medical longitudinal study. Here, our data consists of successive scans of the liver taken during a radio-frequency ablation procedure as described in Sec. IV. Our goal is to to track the position of the needle in a relatively stationary background, while simultaneously reducing sub-sampling artefacts. Specifically, we choose slices 1-6 as our object-prior, and reconstruct slice 7 from few-views with the specific goal of tracking the needle and simultaneously reducing artefacts. Fig. 9 and Fig. 10 show reconstruction of the test slice from its measurements from only 30 views and a zoomed-in version around the RoI. The reconstructions are quantitatively compared using SSIM.

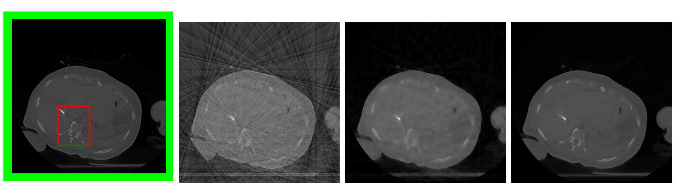

(a) Test (b) FBP (c) TV (d) Spatially varying prior

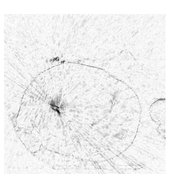

(e) Weights map

Fig. 9: Reconstruction of 'test' (slice 7) from Fig. 3 from only 30 views, using (b) FBP and no prior resulting in streaks (c) TV resulting in blurred bone structures and (d) spatially varying object-prior (slices 1-6 of Fig. 3 are used as object-prior) resulting in clear bone structures with less streaks. The region enclosed in red rectangle is our Region of Interest (RoI) as it contains both the new position of the needle and some background. (e) shows the computed weights map used for reconstruction. Darker intensities indicate lower weights to prior as these are the regions of new changes.

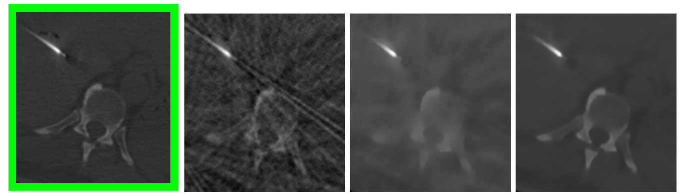

(a) Test (b) FBP (c) TV (d) Spatially varying prior

Fig. 10: A zoomed-in version of the regions around the RoI of the reconstructions shown in Fig. 9.

TABLE II: SSIM of 2D reconstruction of radio-frequency ablation data from various methods. Values have been computed within the RoI. For ground-truth (ideal reconstruction), SSIM equals 1.

	Backprojection	**TV**	**Spatially Varying prior + TV**
2D	0.73	0.91	0.95

*1) **Okra**:* The test volume was reconstructed from a partial set of 45 real cone-beam projections, i.e., 10% of the projection views from which ground truth was reconstructed. 2D reconstructions of one of the slices is shown in Fig. 11. A complete 3D reconstruction can be found in in the supplementary material [31]. The red RoI in the video and images show the regions where new changes are present. A zoomed-in region around the major region of change (red RoI) is shown in Fig. 12. As in the test, the reconstruction by spatially-varying method shows the absence of the deformity and better removal of sub-sampling artefacts when compared to FDK and TV. This is also seen in the SSIM values in Table III.

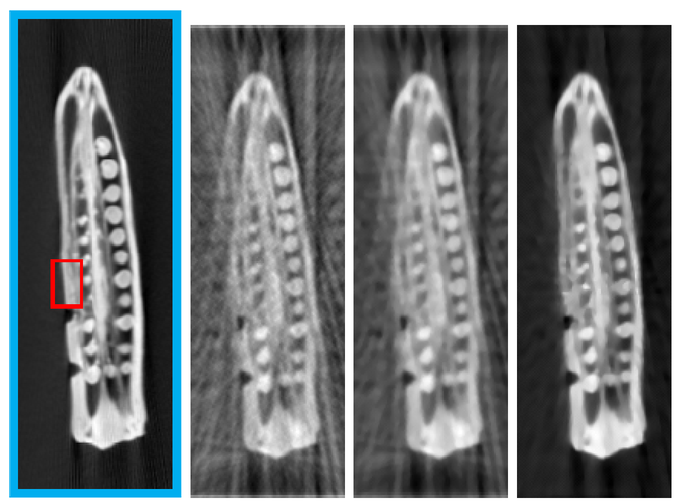

(a) Test (b) FBP, no prior (c) TV, no prior (d) Spatially-Varying prior

Fig. 11: Reconstruction of 2D okra from 48 projection views (b) has streaky artefacts, (c) has blurred structures and (d) is sharper with significantly less streaky artefacts. 3D reconstructed volumes can be viewed in the supplementary material [31].

*2) **Sprouts**:* The test volume was reconstructed from partial set of 45 real cone-beam projections, i.e., 2.5% of the projection views from which ground truth was reconstructed. The selected 3D ground truth of template volumes, test volume, as well as the 3D reconstructions are shown in the supplementary material [31]. 2D reconstruction of one of the slices and a

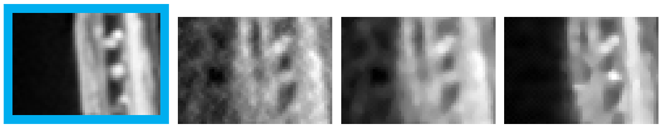

(a) Test (b) FBP, no prior (c) TV, no prior (d) Spatially-Varying prior

Fig. 12: A zoomed-in version of the regions around the RoI of the reconstructions shown in Fig. 11.

TABLE III: SSIM of reconstructed okra from various methods. For 3D, the RoI spans 7 consecutive slices where the test is different from all of the previously scanned objects. SSIM of ground-truth (ideal reconstruction) is 1.

	Backprojection	**TV**	**Spatially Varying prior + TV**
2D	0.46	0.50	0.74
3D	0.69	0.74	0.78

zoomed-in region around the RoI are shown in Figs. 13 and 14 respectively. For the sake of exposition, the red region of interest (RoI) has been culled out from 7 consecutive slices in the 3D volume to indicate new structures; other changes can be viewed in the video. Table IV shows the improvement in SSIM of the reconstructed new regions as compared to other methods.

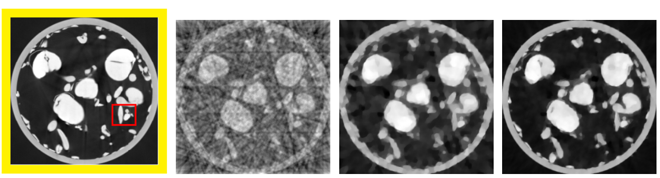

(a) Test (b) FDK, no prior (c) TV, no prior (d) Spatially-Varying prior

Fig. 13: Reconstruction of 2D sprouts from 20 projection views (b) has streaky artefacts, (c) has blurred structures and (d) is sharper with significantly less streaky artefacts. 3D reconstructed volumes can be viewed in the supplementary material [31].

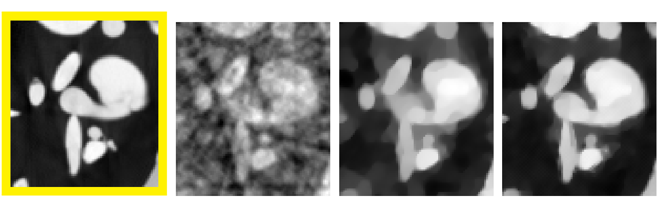

(a) Test (b) FDK, no prior (c) TV, no prior (d) Spatially-Varying prior

Fig. 14: A zoomed-in version of the regions around the RoI of the reconstructions shown in Fig. 13

TABLE IV: SSIM of reconstructed sprouts from various methods. For 3D, the RoI spans 7 consecutive slices where the test is different from all of the previously scanned objects. The SSIM of ground-truth (ideal reconstruction) is 1.

	Backprojection	**TV**	**Spatially Varying prior + TV**
2D	0.67	0.82	0.86
3D	0.67	0.73	0.82

B. *Potato*

The test volume was reconstructed from a partial set of 45 real cone-beam projections, i.e., 5% of the projection views from which ground truth was reconstructed. 2D reconstructions of one of the slices is shown in Fig. 15. A complete 3D reconstruction can be found in the supplementary material [31]. The red RoI in the video and images show regions where both new changes and some old regions are present. The zoomed-in images around the major region of change (red RoI) is shown in Fig. 16.We observe that our method reconstructs new structures while simultaneously reducing streak artefacts. Table V shows SSIM of the reconstructed new regions using various methods.

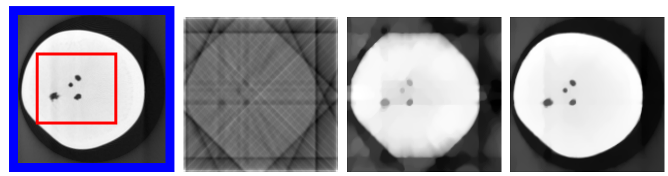

(a) Test (b) FDK, no prior (c) TV, no prior (d) Spatially-Varying prior

Fig. 15: Reconstruction of the 2D-potato from 6 projection views– (b) has strong streak artefacts with unclear structure of the potato, (c) largely blurred, and (c) is sharper with significantly reduced streak artefacts. The 3D reconstructed volumes can be viewed in the supplementary material [31].

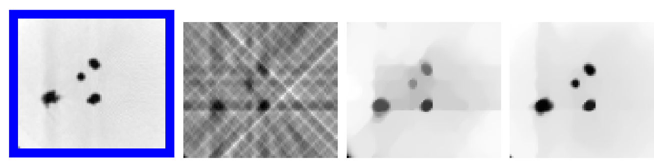

(a) Test (b) FDK, no prior (c) TV, no prior (d) Spatially-Varying prior

Fig. 16: A zoomed-in version of the regions around the RoI of the reconstructions shown in Fig. 15.

TABLE V: SSIM of reconstructed potato from various methods. For 3D, the RoI spans 7 consecutive slices where the test is different from all of the previously scanned objects. SSIM of ground-truth (ideal reconstruction) is 1.

	Backprojection	**TV**	**Spatially Varying prior + TV**
2D	0.52	0.92	0.97
3D	0.58	0.75	0.84

VII. Discussion

In this section, we discuss tuning of the parameters used in our method. λ_1, λ_2 and k are the three hyper-parameters that need to be chosen carefully for optimal reconstruction. In our experiments, λ_1 was tuned to maximize SSIM of the whole reconstructed test volume for TV reconstruction of each dataset. This value was retained for spatially-varying prior-based reconstruction as well. The value of λ_2 largely depends on the amount of artefacts we aim to remove by using object-prior at the cost of their dominance in the new regions. This value was chosen to lie between $0 - 3$ for our datasets. Finally, the hyper-parameter k defines the sensitivity of the weights map to the difference between test image and object-prior (projection of test onto the space of object-prior). When $k = 0$, our method behaves similar to the uniform prior method discussed in [35]. As k increases, the weights map starts capturing new changes in the test, at the cost of detecting a few false positives i.e., false new changes. In other words, as the weights-map becomes more sensitive to the difference between the test and object-prior, it becomes more noisy. In order to visualize the effect of the hyper-parameter k, we performed 2D reconstructions on okra dataset for different values of k. Fig. 17 shows the weights map obtained for each of the k values and Fig. 18 shows the corresponding final reconstructions. We run our experiments for a few values of k and choose the best reconstruction based on our tolerance for noise in the weights-map. When a large number of templates are available, this parameter can be chosen by assuming one of the templates as test and choosing the k that gave the best reconstruction. Alternatively, in cases where one wishes to completely avoid the use of this hyper-parameter, one can construct a binary weights-map using a learning based method described in the supplementary material [31].

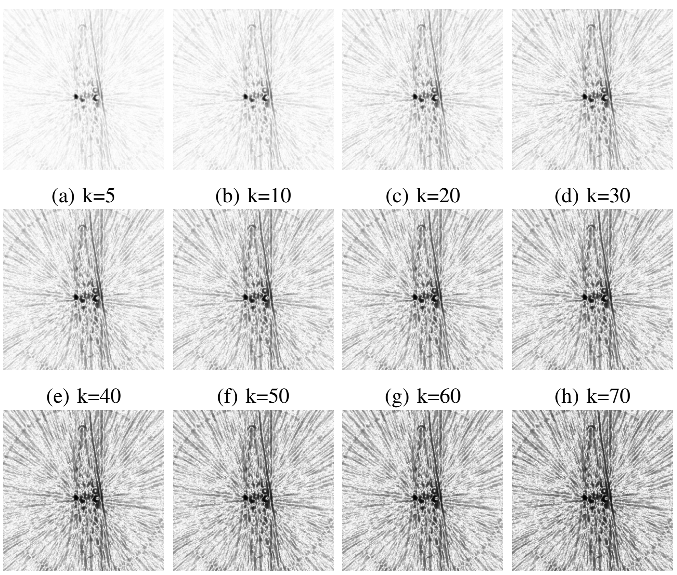

(a) k=5 (b) k=10 (c) k=20 (d) k=30

(e) k=40 (f) k=50 (g) k=60 (h) k=70

(i) k=80 (j) k=90 (k) k=100 (l) k=130

Fig. 17: Different weights-maps for okra reconstruction. Low intensity denotes regions of new changes in test.

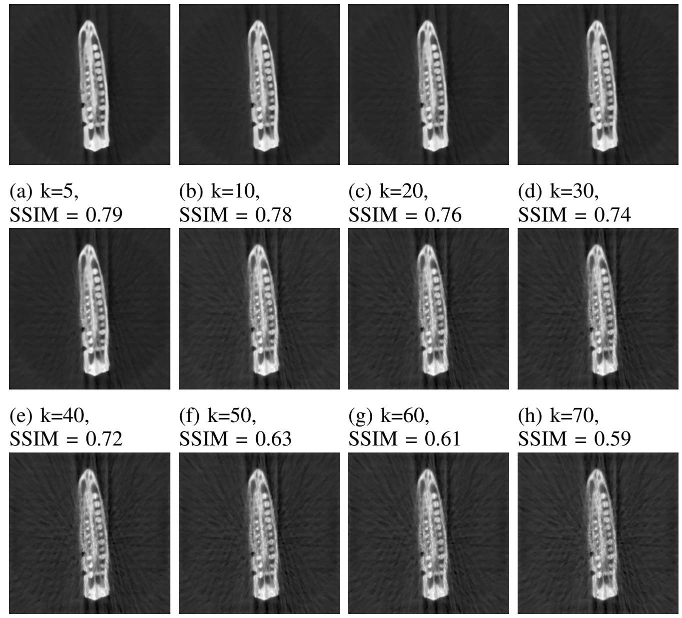

(a) k=5, SSIM = 0.79 (b) k=10, SSIM = 0.78 (c) k=20, SSIM = 0.76 (d) k=30, SSIM = 0.74

(e) k=40, SSIM = 0.72 (f) k=50, SSIM = 0.63 (g) k=60, SSIM = 0.61 (h) k=70, SSIM = 0.59

(i) k=80, SSIM = 0.58 (j) k=90, SSIM = 0.56 (k) k=100, SSIM = 0.55 (l) k=130, SSIM = 0.53

Fig. 18: 2D reconstructions for varying values of k. The SSIM values for all images are computed within the red RoI (shown in Fig. 11(a)), the region where the test is different from all of the previously scanned objects.

VIII. Conclusions

This work deals with the effective use of priors for tomographic reconstruction in longitudinal studies. When the number of measurements is substantially low, we discuss the utility of using information from previous scans of the same object, as outlined in Fig. 2. In order to observe details of new changes accurately, we use a novel spatially-varying prior-based method. This method ensures that the reconstruction of localized new information in the data is not affected by the priors, while the other relatively stationary regions benefit from the extra prior information. We have thus improved state of the art by detecting the strength and location of these regions of change and assigning low prior weights wherever necessary. The probability of presence of a 'new region' is enhanced considerably by a novel combination of different reconstruction techniques. We have validated our technique on medical 2D and real, biological 3D datasets for longitudinal studies. The method is also largely robust to the number of previously scanned objects used. We urge the reader to see the videos of reconstructed volumes in the supplementary material [31].

IX. Acknowledgement

We are grateful to Dr. Andrew Kingston for facilitating data collection at the Australian National University. AR gratefully acknowledges IITB Seed-grant 14IRCCSG012, as well as NVIDIA Corporation for the generous donation of a Titan-X GPU card, which was essential for computing 3D reconstructions for the research reported here. We also thank Dr. Akshay Baheti for providing us with medical data from Tata Memorial Hospital, Mumbai.

References

[1] X. Yang, V. De Andrade, W. Scullin, E. L. Dyer, N. Kasthuri, F. De Carlo, and D. Gürsoy, "Low-dose X-ray tomography through a deep convolutional neural network," *Scientific Reports*, vol. 8, no. 1, 2018.

[2] L. Fu *et al.*, "Comparison between pre-log and post-log statistical models in ultra-low-dose CT reconstruction," *IEEE transactions on medical imaging*, vol. 36, no. 3, pp. 707 – 720, 2016.

[3] Q. Xie, D. Zeng, Q. Zhao, D. Meng, Z. Xu, Z. Liang, and J. Ma, "Robust low-dose CT sinogram preprocessing via exploiting noise-generating mechanism," *IEEE Transactions on Medical Imaging*, vol. 36, no. 12, pp. 2487–2498, Dec 2017.

[4] P. Gopal, S. Chandran, I. Svalbe, and A. Rajwade, "Low radiation tomographic reconstruction with and without template information," *Signal Processing*, vol. 175, p. 107582, 2020.

[5] A. M. Kingston, G. R. Myers, S. J. Latham, B. Recur, H. Li, and A. P. Sheppard, "Space-filling X-ray source trajectories for efficient scanning in large-angle cone-beam computed tomography," *IEEE Transactions on Computational Imaging*, vol. 4, no. 3, pp. 447–458, Sep. 2018.

[6] A. Cazasnoves, S. Sevestre, F. Buyens, and F. Peyrin, "Statistical content-adapted sampling (SCAS) for 3D computed tomography," *Computers in Biology and Medicine*, vol. 92, pp. 9 – 21, 2018.

[7] O. Barkan, J. Weill, S. Dekel, and A. Averbuch, "A mathematical model for adaptive computed tomography sensing," *IEEE Transactions on Computational Imaging*, vol. 3, no. 4, pp. 551–565, Dec 2017.

[8] A. Fischer, T. Lasser, M. Schrapp, J. Stephan, and P. B. Noël, "Object specific trajectory optimization for industrial X-ray computed tomography," *Scientific Reports*, vol. 6, no. 19135, Jan 2016.

[9] A. Dabravolski, K. J. Batenburg, and J. Sijbers, "Dynamic angle selection in X-ray computed tomography," *Nuclear Instruments and Methods in Physics Research Section B: Beam Interactions with Materials and Atoms*, vol. 324, pp. 17 – 24, 2014, 1st International Conference on Tomography of Materials and Structures.

[10] L. L. Geyer, U. J. Schoepf, F. G. Meinel, J. W. Nance, G. Bastarrika, J. A. Leipsic, N. S. Paul, M. Rengo, A. Laghi, and C. N. De Cecco, "State of the art: Iterative CT reconstruction techniques," *Radiology*, vol. 276, no. 2, pp. 339–357, 2015.

[11] K. Kilic, G. Erbas, M. Guryildirim, M. Arac, E. Ilgit, and B. Coskun, "Lowering the dose in head CT using adaptive statistical iterative reconstruction," *American Journal of Neuroradiology*, vol. 32, no. 9, pp. 1578–1582, 2011.

[12] L. I. Rudin, S. Osher, and E. Fatemi, "Nonlinear total variation based noise removal algorithms," *Physica D: Nonlinear Phenomena*, vol. 60, no. 1, pp. 259–268, 1992.

[13] D. Donoho, "Compressed sensing," *IEEE Transactions on Information Theory*, vol. 52, no. 4, pp. 1289–1306, April 2006.

[14] E. Candès and M. Wakin, "An introduction to compressive sampling," *IEEE Signal Proc. Mag.*, vol. 25, no. 2, pp. 21–30, March 2008.

[15] T. L. Jensen, J. H. Jørgensen, P. C. Hansen, and S. H. Jensen, "Implementation of an optimal first-order method for strongly convex total variation regularization," *BIT Numerical Mathematics*, vol. 52, pp. 329–356, 2012.

[16] Tobias Lindstrøm Jensen and Jakob Heide Jørgensen and Per Christian Hansen and Søren Holdt Jensen, "TV-Regularization Library," https://github.com/jakobsj/TVReg, last viewed–August, 2021.

[17] E. A. Rashed, M. al Shatouri, and H. Kudo, "Sparsity-constrained three-dimensional image reconstruction for C-arm angiography," *Computers in Biology and Medicine*, vol. 62, pp. 141 – 153, 2015.

[18] L. Liu, W. Lin, and M. Jin, "Reconstruction of sparse-view X-ray computed tomography using adaptive iterative algorithms," *Computers in Biology and Medicine*, vol. 56, pp. 97 – 106, 2015.

[19] A. G. Polak, J. Mroczka, and D. Wysoczański, "Tomographic image reconstruction via estimation of sparse unidirectional gradients," *Computers in Biology and Medicine*, vol. 81, pp. 93 – 105, 2017.

[20] G.-H. Chen, J. Tang, and S. Leng, "Prior image constrained compressed sensing (PICCS): A method to accurately reconstruct dynamic CT images from highly undersampled projection data sets," *Medical Physics*, vol. 35, no. 2, pp. 660–663, 2008.

[21] J. W. Stayman, H. Dang, Y. Ding, and J. H. Siewerdsen, "PIRPLE: A penalized-likelihood framework for incorporation of prior images in CT reconstruction," *Physics in medicine and biology*, vol. 58, no. 21, pp. 7563–82, Nov 2013.

[22] K. Ruymbeek and W. Vanroose, "Algorithm for the reconstruction of dynamic objects in CT-scanning using optical flow," *Journal of Computational and Applied Mathematics*, vol. 367, p. 112459, 2020.

[23] V. V. Nieuwenhove, "Model-based reconstruction algorithms for dynamic X-ray CT," Ph.D. dissertation, University of Antwerp, 2017.

[24] D. Kazantsev, W. M. Thompson, W. R. B. Lionheart, G. V. Eyndhoven, A. P. Kaestner, K. J. Dobson, P. J. Withers, and P. D. Lee, "4D-CT reconstruction with unified spatial-temporal patch-based regularization," p. 447, 2015.

[25] G. Van Eyndhoven, K. J. Batenburg, D. Kazantsev, V. Van Nieuwenhove, P. D. Lee, K. J. Dobson, and J. Sijbers, "An iterative CT reconstruction algorithm for fast fluid flow imaging," *IEEE Transactions on Image Processing*, vol. 24, no. 11, pp. 4446–4458, 2015.

[26] M. Heyndrickx, T. D. Schryver, M. Dierick, M. Boone, T. Bultreys, V. Cnudde, and L. V. Hoorebeke, "Improving the reconstruction of dynamic processes by including prior knowledge," *HD-Tomo-Days, Abstracts.*, 2016.

[27] Z. S. Hao Gao, Jian-Feng Cai and H. Zhao, "Robust principal component analysis-based four-dimensional computed tomography," *Physics in Medicine and Biology*, vol. 56, no. 11, pp. 3181–98, Jun 7 2011.

[28] V. E. G, B. KJ, and S. J., "Region-based iterative reconstruction of structurally changing objects in CT," *IEEE Trans Image Process.*, vol. 23, no. 2, pp. 909–919, 2014.

[29] A. Pourmorteza, H. Dang, J. H. Siewerdsen, and J. W. Stayman, "Reconstruction of difference using prior images and a penalized-likelihood framework," *International Meeting on Fully Three-Dimensional Image Reconstruction in Radiology and Nuclear Medicine*, p. 252–257, 2015.

[30] J. Lee, J. W. Stayman, Y. Otake, S. Schafer, W. Zbijewski, A. J. Khanna, J. L. Prince, and J. H. Siewerdsen, "Volume-of-change cone-beam CT for image-guided surgery," pp. 4969–89, Aug 2012.

[31] Supplemental material for 'Eliminating object prior-bias from sparse-projection tomographic reconstructions', "in Dropbox," https://www.dropbox.com/sh/sn9mvhym3sv4pjb/AABLmnvlnVReBQj-0miSn73Ba?dl=0, Including video reconstruction results.

[32] "Tata Memorial Centre," https://en.wikipedia.org/wiki/Tata_Memorial_Centre, Wikipedia.

[33] J. Dong, W. Li, Q. Zeng, S. Li, X. Gong, L. Shen, S. Mao, A. Dong, and P. Wu, "CT-guided percutaneous step-by-step radiofrequency ablation for the treatment of carcinoma in the caudate lobe," *Medicine*, vol. 94, no. 39, 2015.

[34] L. Feldkamp, L. C. Davis, and J. Kress, "Practical cone-beam algorithm," *J. Opt. Soc. Am*, vol. 1, pp. 612–619, 01 1984.

[35] P. Gopal, R. Chaudhry, S. Chandran, I. Svalbe, and A. Rajwade, "Tomographic reconstruction using global statistical priors," in *DICTA*, Sydney, Nov. 2017.

[36] R. Meyer, "Sufficient conditions for the convergence of monotonic mathematical programming algorithms," *Journal of Computer and System Sciences*, vol. 12, no. 1, pp. 108 – 121, 1976.

[37] R. Tibshirani, "Regression shrinkage and selection via the Lasso," *Journal of the Royal Statistical Society. Series B (Methodological)*, vol. 58, no. 1, pp. 267–288, 1996.

[38] R. Gordon, R. Bender, and G. T. Herman, "Algebraic reconstruction techniques (ART) for three-dimensional electron microscopy and X-ray photography," *Theoretical Biology*, vol. 29, no. 3, pp. 471–481, Dec 1970.

[39] A. Andersen and A. Kak, "Simultaneous algebraic reconstruction technique (SART): A superior implementation of the ART algorithm," *Ultrasonic Imaging*, vol. 6, no. 1, pp. 81 – 94, 1984.

[40] P. Gilbert, "Iterative methods for the three-dimensional reconstruction of an object from projections," *Journal of Theoretical Biology*, vol. 36, no. 1, pp. 105 – 117, 1972.